AGU PUBLICATIONS

JGR

Journal of Geophysical Research: Oceans

RESEARCH ARTICLE

10.1002/2014JC009831

Coastal cape and canyon effects on wind-driven upwelling in northern Taiwan Strait

Zhaoyun Chen[1,2], Xiao-Hai Yan[2,3], and Yuwu Jiang[1,2]

[1]State Key Laboratory of Marine Environmental Science, Xiamen University, Xiamen, Fujian, China, [2]University of Delaware/Xiamen University Joint Institute for Coastal Research and Management (Joint-CRM), Newark, Delaware, USA/ Xiamen, China, [3]Center for Remote Sensing, College of Earth, Ocean and Environment, University of Delaware, Newark, Delaware, USA

Key Points:
- We observe an upwelling strip with two cores in northern Taiwan Strait
- Mechanisms of these upwelling structures are explored
- Relative vorticity change dominates vertical velocity off cape and canyon

Correspondence to:
Y. Jiang,
ywjiang@xmu.edu.cn

Citation:
Chen, Z., X.-H. Yan, and Y. Jiang (2014), Coastal cape and canyon effects on wind-driven upwelling in northern Taiwan Strait, *J. Geophys. Res. Oceans*, *119*, 4605–4625, doi:10.1002/ 2014JC009831.

Received 18 JAN 2014
Accepted 9 JUL 2014
Accepted article online 12 JUL 2014
Published online 31 JUL 2014

Abstract A combination of observations and numerical model is used to reveal the upwelling features and mechanisms in the northern Taiwan Strait during summer. In situ data give evidence of the upwelling in the form of thermocline tilting upward onshore. The remote sensing data show a strip of upwelling in the coastal region, which occurs more than half a summer. The upwelling probability map indicates there are two upwelling cores, one located downstream of Pingtan Island formed as cape effect and the other over the coastal canyon off the Sansha Bay. Remote sensing data and numerical model results suggest that the southerly wind plays a key role in shaping this upwelling strip, while the tides regulate the upwelling location through tidal mixing effect in the shallow water region, especially lee of Pingtan Island. Further numerical experiments using idealized cape and coastal canyon topography show that vertical velocity is intensified downstream of the cape and canyon. The vorticity equation shows that relative vorticity change along a streamline and frictional diffusion of vorticity are responsible for the vertical velocity off the cape and within and around the canyon. According to the conservation of potential vorticity, the variation of relative vorticity along a streamline over irregular topography, e.g., cape and canyon, is the main mechanism for the two upwelling cores in the northern Taiwan Strait.

1. Introduction

Coastal upwelling is a circulation along the coast, which brings subsurface cold and nutrient rich water up to the euphotic zone, and induces water divergences in the surface layer. For wind-driven coastal upwelling, its intensity is closely related to wind stress [*Samelson et al*., 2002; *Wang et al*., 2014], upwelling favorable wind duration [*Breaker and Mooers*, 1986], coastline geometry [*Rodrigues and Lorenzzetti*, 2001], and the inner shelf [*Austin and Lentz*, 2002]. Thus, *Jiang et al*. [2012] and *Chen et al*. [2013a] proposed an upwelling index, upwelling age, which contains the effects of the alongshore wind stress, the shelf slope, and the wind duration, to evaluate the upwelling intensity off the coast with different circumstances.

Upwelling band can be rearranged by cape and shelf of changing width. *Arthur* [1965] estimated the relative vorticity along a streamline to explain the enhanced upwelling downstream of a cape using a simplified vorticity equation. Enhanced upwelling lee of the cape is observed by hydrographic survey, satellite, and is reproduced by numerical model [*Doglioli et al*., 2004; *Williams and Carmack*, 2008; *Mason et al*., 2012]. Onshelf (downslope) transport is enhanced over a widened shelf downwind during upwelling- (downwelling-) favorable wind event, rendering an intensified upwelling (downwelling) circulation over the inner shelf [*Pringle*, 2002; *Gan et al*., 2009, 2013].

Submarine canyon topography can alter the circulation and mass exchange within and around the canyon, which has received much attention from oceanographers. The up-shelf transport downstream of the submarine canyon is 1 order of magnitude larger than that over the shelf break [*Allen*, 1996; *Klinck*, 1996]. Dense water with massive sediment from the deep ocean is transported to the continental shelf along the submarine canyon. Canyon upwelling flux depends on along-slope flow speed, flow direction, canyon depth, and stratification [*Klinck*, 1996; *Kämpf*, 2007]. Stratification leads to the formation of a cyclonic eddy over the canyon, and restricts the vertical scope of canyon effect [*Klinck*, 1996; *Kämpf*, 2007]. *Klinck* [1996] demonstrated that the interaction of pressure gradient and Coriolis acceleration by the bathymetric gradient rather than

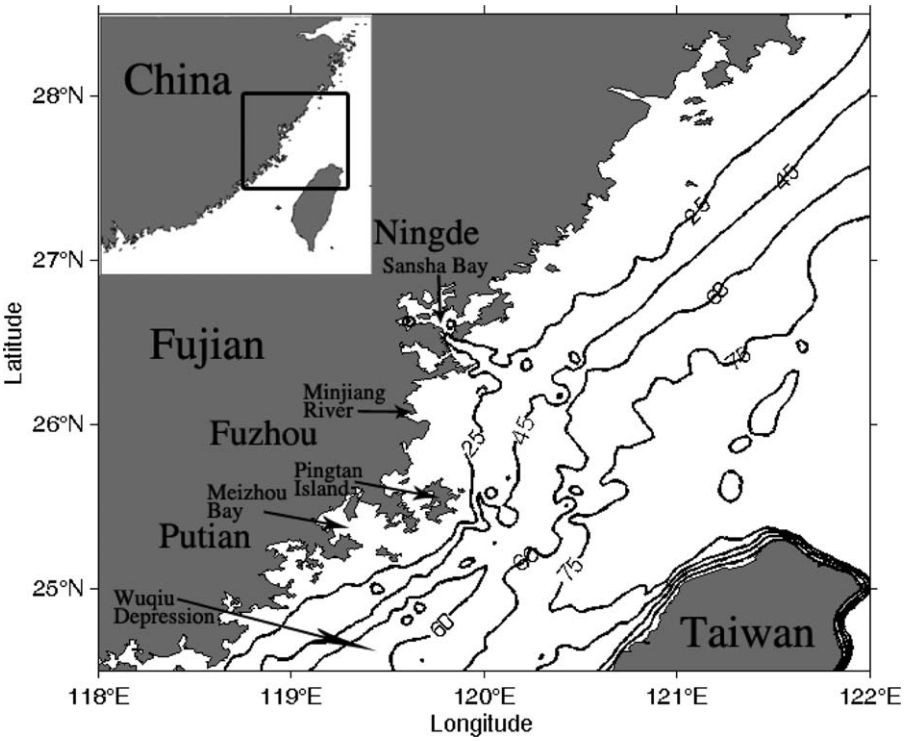

Figure 1. The bathymetry (in meters) in the northern Taiwan Strait. The inset in the top-left corner is the zoomed out area off southeast China coast.

momentum advection determined the circulation over the canyon, while *She and Klinck* [2000] showed that the momentum advection was important in creating the circulation over the canyon. Cross-shelf flow induced by a submarine canyon may be extended to a considerable distance along the shelf, and a headland located downstream of the canyon can enhance the cross-shelf flow, which results in the formation of a stationary coastal upwelling core [*Kämpf*, 2012]. Although the dynamics over submarine canyon are well studied, the circulation over coastal canyon and its response to surface wind are still unknown.

The Taiwan Strait (TWS) is a channel for the water exchange between the East China Sea and the South China Sea. The TWS is dominated by the East Asia monsoon. From mid-September to April, the northeasterly winds prevail; and from June to August, the winds are reversed [*Hellerman and Rosenstein*, 1983; *Jan et al*., 2002]. The South China Sea Warm Current extends northeastward in the western and central TWS, and the branch of the Kuroshio Loop Current exists in the eastern TWS [*Hu et al*., 2010]. The submarine topography in the northern TWS is characterized by the broad continental shelf as shown in Figure 1. One can see that a shoreward convex of 25 m isobath exists off the Sansha Bay, forming a feature of coastal canyon. The seaward protruding Pingtan Island makes the isobaths concave seaward. The diluted water from the Minjiang River fluxes out between them. Because of the shallow water depth and short distance between the main land and Pingtan Island, the island can be regarded as a cape affecting on the coastal circulation. To the south of Pingtan Island, a strip-shaped structure of 60 m isobath is the Wuqiu Depression, through which the northward undercurrent brings the subsurface water up-climbing to the shallow shelf.

For the evidence of upwelling in the northern TWS, early oceanographers used in situ hydrographic observations. *Xiao* [1988], *Huang* [1989a, 1989b], and *Chen et al*. [2001] defined an upwelling core off Pingtan Island, and showed that this upwelling appeared from June to August. The upwelling exhibits the strongest intensity in July, and the temperature drop in the upwelling area reaches 1.5–3.0°C comparing to the surrounding sea water [*Weng et al*., 1992; *Hu et al*., 2000]. Later, with the available of remote sensing data, low-temperature area revealed by the remote sensing data provided a clear evidence for the upwelling there [*Hu et al*., 2001; *Tang et al*., 2002].

For mechanisms of the upwelling off Pingtan Island based on the analysis of cruise data, *Xiao* [1988], *Huang* [1989a], and *Huang and Weng* [1996] pointed out that the prevailing southwesterly wind and the northward

ascending bottom current located in the Wuqiu Depression played the major roles in forming the upwelling. Through estimating of the order of vertical velocity induced by the current, the wind, and the tidal mixing, *Wu et al*. [1997] revealed that the dominated factor for the generation of this upwelling was interaction of the bathymetry and the northward current. The northward subsurface water flowing through the Wuqiu Depression compensates the offshore Ekman transport caused by the southwesterly monsoon, and forms the upwelling off Pingtan Island [*Liang*, 1997]. All of these hypotheses of mechanisms were based on in situ observations, while *Yan et al*. [1997] proposed that upwelling off the Fujian coast was intensified by the prevailing southwesterly monsoon using a 3-D numerical model. Due to the advance of numerical modeling and computing power, further understanding of the mechanism of the upwelling core off Pingtan Island, as well as the reasons for the spatial structures of upwelling beyond Pingtan Island in the northern TWS, is possible.

In this study, a combination of in situ observation, remote sensing data, and numerical model with both realistic and idealized conditions is used to systematically study the upwelling features and mechanisms in the northern TWS. The vorticity equation is used to reveal why the upwelling is intensified downstream of the cape and coastal canyon under upwelling favorable wind, so as to explain the resultant upwelling features in the northern TWS.

2. Data, Theory, and Numerical Model

2.1. Hydrological Survey and Satellite Data

During 25 June to 7 July, 2012, a cruise was carried out in the western TWS by Xiamen University, with a focus on upwelling in the southwestern TWS, the Taiwan Bank, and the northern TWS. In this study, the measurements in the northern TWS are used. Temperature and salinity from surface to bottom at each station were measured by an SBE 917 CTD profiler. Surface temperature and salinity were measured at 10 s interval along the cruising route by SBE 21 Thermosalinograph. Data at each station and along the cruise route are interpolated to make section profile and surface distribution using Kriging interpolation method. At each sampling station, only the CTD data during hauling up stage are used.

The wind used to force the numerical model and analyze its effect on the upwelling is from the QuikSCAT, which is available from June 1999 to November 2009. The QuikSCAT data set provides ascending and descending passes of zonal and meridional components of surface wind. The global wind data with a 0.25° resolution are available from the Jet Propulsion Laboratory website (http://podaac.jpl.nasa.gov/). Climatological monthly mean wind data (9 year averaged using 2000–2008 data) are interpolated to the model grids to simulate the climatological features of upwelling in the northern TWS. Daily averaged wind data in July 2008, combined with the SST images, are used to discuss the important effect of the wind.

The MODIS sensor provides an accurate and high-resolution representation of the SST field. Aqua daytime SST data from the OceanColor website (http://oceancolor.gsfc.nasa.gov/) with a 4 km resolution are used to study the upwelling events. The images used here are the 8 day averaged Level-3 gridded data from 2002 to 2012 in the northern TWS (119–121.5°E, 25–27.5°N) in summer. Climatological monthly mean SST data in July are also used to show the spatial distribution of the upwelling features in the study area.

2.2. Vorticity Equation

The estimate of vertical velocity from the horizontal motion used here is from *Arthur* [1965]. The momentum equations are

$$\frac{Du}{Dt} = fv - \frac{1}{\rho}\frac{\partial p}{\partial x} + F_x,$$
$$\frac{Dv}{Dt} = -fu - \frac{1}{\rho}\frac{\partial p}{\partial y} + F_y \tag{1}$$

where u and v are the horizontal velocity in the x and y directions, respectively, f is the Coriolis parameter, p is the pressure, ρ is the water density, and F_x and F_y are the friction terms in the x and y directions, respectively. The continuity equation is

$$\frac{\partial w}{\partial z}+\frac{\partial u}{\partial x}+\frac{\partial v}{\partial y}=0, \tag{2}$$

where w is the vertical velocity and z is the vertical coordinate. Cross differentiating the momentum equations in combination with the continuity equation under the assumption of constant eddy viscosity, the horizontal divergence term can be written as

$$\begin{aligned}(f+\zeta)\frac{\partial w}{\partial z}=\frac{D\zeta}{Dt}+\beta v-\left(\frac{\partial w}{\partial y}\frac{\partial u}{\partial z}-\frac{\partial w}{\partial x}\frac{\partial v}{\partial z}\right)-w\left(\frac{\partial^2 u}{\partial y\partial z}-\frac{\partial^2 v}{\partial x\partial z}\right)\\ -\left(\frac{\partial p}{\partial x}\frac{\partial \rho^{-1}}{\partial y}-\frac{\partial p}{\partial y}\frac{\partial \rho^{-1}}{\partial x}\right)-A_H\left(\frac{\partial^2\zeta}{\partial x^2}+\frac{\partial^2\zeta}{\partial y^2}\right)-A_z\frac{\partial^2\zeta}{\partial z^2},\end{aligned} \tag{3}$$

where $\zeta=\partial v/\partial x-\partial u/\partial y$ is the vorticity, β is the β-plane approximation, A_H is the horizontal eddy viscosity, and A_z is the vertical eddy viscosity. Taking an f-plane approximation for a barotropic flow in a steady state and neglecting the horizontal friction term, the horizontal divergence equation can be simplified to

$$(f+\zeta)\frac{\partial w}{\partial z}=u\frac{\partial\zeta}{\partial x}+v\frac{\partial\zeta}{\partial y}-A_z\frac{\partial^2\zeta}{\partial z^2}. \tag{4}$$

Then, integrating the above equation vertically and taking the surface vertical velocity $w_0=0$, the vertical velocity at each z-level is

$$w_z=-\int_z^0\frac{1}{f+\zeta}\left(u\frac{\partial\zeta}{\partial x}+v\frac{\partial\zeta}{\partial y}\right)dz+\int_z^0\frac{A_z}{f+\zeta}\frac{\partial^2\zeta}{\partial z^2}dz, \tag{5}$$

where the first term is related to spatial relative vorticity change along a streamline (RVC) and the second term is the vertical velocity induced by frictional diffusion of vorticity (FDV). Note that the surface boundary condition for the second term is zero, because no Ekman pumping is included in the idealized numerical model experiments. Equation (5) is in analogy with the potential vorticity conservation equation when the second term is excluded, meaning if the relative vorticity changes along a streamline, the water column will stretch or squeeze, resulting in vertical velocity change. Consistently, the constraint of potential vorticity conservation requires current flowing along the constant contour of potential vorticity, $(f+\zeta)/H$, where H is the water depth. When the current encounters irregular bathymetry, such as coastal cape or canyon, it will move to deep ocean or shallow shelf with the varying relative vorticity, keeping potential vorticity conservation.

2.3. Numerical Model Configurations and Control Experiments

The Regional Ocean Modeling System (ROMS) is used to explore the upwelling process and its mechanisms. The model employs nested curvilinear grids to ensure a proper simulation of the upwelling features in the region (Figure 2). The coarse grid covers the northwestern Pacific extending from (99°E, 9°S) in the southwest to (148°E, 44°N) in the northeast with a varying resolution from 1/3° at the open boundary to 1/50° in the TWS. The fine-grid model domain covers the northern TWS extending from (117.5°E, 24°N) in the southwest to (123°E, 29.5°N) in the northeast with a highest resolution of ~0.7 km off the Sansha Bay. The coarse-grid model has 30 vertical terrain-following σ-levels, and the fine-grid model has 25 vertical levels. Both models are configured with more grid points concentrated in the surface layer. The initial and boundary conditions of the coarse-grid model are extracted from the World Ocean Atlas (WOA) 2005, and the surface heat flux is obtained from the Comprehensive Ocean-Atmosphere Data Set (COADS05) [*Da Silva et al.*, 1994]. The model domain has only one open boundary, for which velocity components, surface elevation, and temperature are interpolated from the WOA, and 10 major tidal components (M_2, S_2, N_2, K_2, K_1, O_1, P_1, Q_1, M_f, and M_m) are derived from the TPXO7.0 [*Egbert and Erofeeva*, 2002]. The climatological monthly mean river discharge from the Minjiang River is included. The models are forced by climatological monthly mean wind from the QuikSCAT. The bathymetry used in the models is derived from a combination of ETOPO2

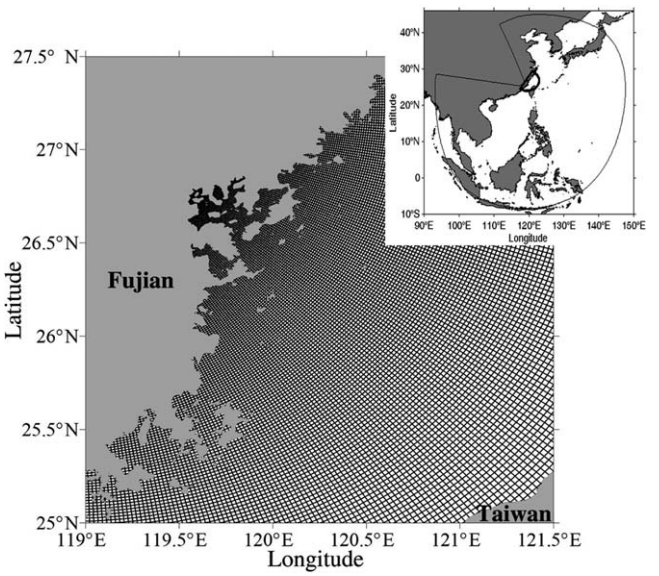

Figure 2. The grids of the fine model for the study region. The top-right inset shows the model domains of coarse grids (thin line) and that of fine grids (thick line).

(from the National Geophysical Data Center, USA) and digitized navigation charts (from the Maritime Safety Administration, China). The radiation condition of *Flather* [1976] is used for the open boundary. The Large McWilliams and Doney (LMD) shear mixing scheme [*Large et al*., 1994] is performed to calculate the vertical turbulent viscosity and diffusion. For more details on model descriptions, readers are referred to *Liao et al*. [2013]. After the coarse-grid model is run for 1 year, the outputs are interpolated to the fine-grid model as boundary and initial conditions. Then, the fine-grid model is run from May to July. Only the fine-grid monthly mean model results in July are presented, representing the typical upwelling event in the northern TWS in summer.

To examine the effects of a cape and a coastal canyon on coastal upwelling, the numerical model is further set up in idealized conditions. Figure 3 gives the schematic of the bathymetry and coastline geometry. The simple configuration of the bathymetry and coastal mask allows us to better understand the mechanisms for the observed features in the northern TWS in summer. The idealized model is configured with land to the west of the western boundary, and the gradient boundary conditions at the northern and southern boundaries, and outward radiation at the open eastern boundary. The model domain is 120 km in the cross-shore direction and 300 km in the alongshore direction, and discretized with a grid resolution of 0.5 km × 0.5 km. The minimum water depth is set to 5 m at the coast, and the bathymetry gradually declines to a flat bottom of $h = 75$ m with a shelf slope of $\alpha = 1.0 \times 10^{-3}$. The cape boundary from the reference coast is shaped according to

$$x* = x_1 \sin\left[\frac{\pi}{y_2}(y - y_1)\right] \text{with } y_1 \le y \le y_1 + y_2, \tag{6}$$

where $x_1 = 25$ km, $y_1 = 90$ km, and $y_2 = 30$ km. In the downstream ($y_3 = 70$ km) of the cape is a coastal canyon, which has a maximum depth of $h_1 = 35$ m. The bathymetry of the canyon is defined as

$$h* = \max\left\{\frac{h_1}{2}\left[1 + \tanh\frac{x - x_0(y)}{15}\right], x\alpha\right\}, \tag{7}$$

in which

$$x_0(y) = x_2\left\{1 - \sin\left[\frac{\pi}{y_4}(y - y_1 - y_2 - y_3)\right]\right\}, \tag{8}$$

with $y_1 + y_2 + y_3 \le y \le y_1 + y_2 + y_3 + y_4$ and $x \le 75$ km. The canyon width is $y_4 = 20$ km and $x_2 = 25$ km is related to the length of the canyon axis. The model uses an *f*-plane approximation with a Coriolis parameter of $f = 6 \times 10^{-5}$ s^{-1}. The initial velocity and surface elevation are set to 0, and the temperature is initialized in the whole model domain in the form of

$$T(z) = 3 \arctan\left(\frac{z + 20}{5}\right) + 26, \tag{9}$$

where z is the depth in meters. The temperature decreases from 30°C at the surface to 26°C at thermocline, and is nearly constant (~22°C) below 35 m. The initially motionless ocean is forced by spatially uniform

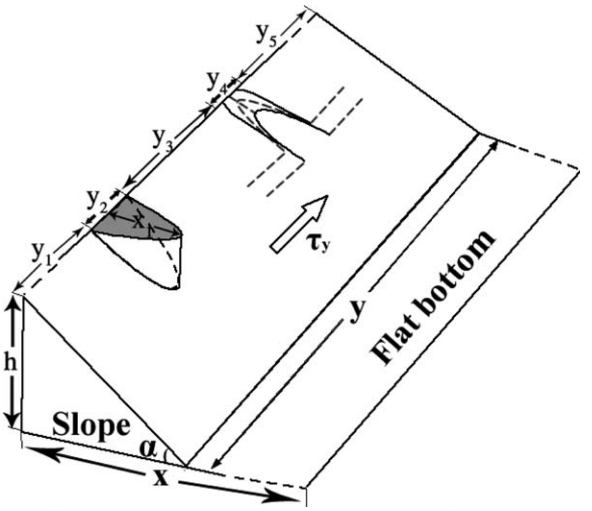

Figure 3. Schematic of the bathymetry with a cape and a canyon. The sine-shaped cape is 70 km south of the sine-shaped canyon. The distance between the cape and the southern boundary is $y_1 = 90$ km, and that between the canyon and the northern boundary is $y_5 = 90$ km.

wind from the south, which gradually increases in time according to $\tau(t) = \tau_0(1 - e^{-3t})$, where t is the time in days, and $\tau_0 = 0.04$ N m^{-2} represents the alongshore wind stress in summer. All these parameters are comparable to those in the northern TWS. For simplicity, the vertical eddy viscosity is fixed to be a constant of $A_z = 6.5 \times 10^{-3}$ m^2 s^{-1} in the idealized model.

Table 1 describes the numerical experiments used to check the effects of wind, tides, cape, and coastal canyon. To reproduce the hydrodynamic conditions in the northern TWS, the model in Case A is forced by climatological monthly mean wind with tidal effect as well as realistic coastline and topography. After successfully reproducing the upwelling characteristics in the northern TWS, the model is used for sensitive experiments. In Case B, tidal effect is removed. In Case C, both wind and tides in the northern TWS in July are not included. Cases D and E are the idealized numerical experiments with only a cape and with only a coastal canyon, respectively, and Case F includes both cape and coastal canyon.

3. Evidence of Upwelling

3.1. Hydrographic Survey Results

Figure 4 shows the surface temperature and salinity distributions on 6 July 2012 near Pingtan Island. The sampling stations are marked by the crosses. Cold upwelled water stretched along the coast in the nearshore region. Cold upwelled water was observed at Stations A2, B1, and C1, and was pronouncedly different to the warm water seaward; however, the high salinity related to the coastal upwelling in the nearshore region is not obvious due to the influence of river discharge. Station A1 is located in the estuary of the Minjiang River, and low-salinity water is observed in the nearby region. Less influenced by river discharge, upwelled water characterized by lower temperature and higher salinity exists between Stations C1 and C2.

The temperature, salinity, and density sections sampled by CTD measurements on 6 July 2012 are shown in Figure 5. In Section A, a dome-shaped thermocline, halocline, and pycnocline are located at Station A2. The 26–27.5°C isotherms outcrop in the region of A2–A3. Low-salinity plume from the Minjiang River is observed in the nearshore region. The river plume overlays on the pycnocline, and is less than 10 m in thickness. In Section B, isotherms are uplifted shoreward, demonstrating that upwelling exists off Pingtan Island (Figure 5d). The freshwater mixes with the upwelled water in the region of B1–B2, resulting in strong thermal wind shear in the water column. In Section C, the pycnocline is raised shoreward, and the upwelled water characterized by lower temperature and higher salinity appears in the nearshore surface layer. The nearshore bottom water below the pycnocline shows lower temperature, higher salinity, and higher density in all three sections, which is transported from the

Table 1. Numerical Experiments With (r) Representing Realistic Model Condition and (i), Idealized Model Condition

Experiment	Description
Case A	Normal (r)
Case B	No tides (r)
Case C	No wind and tides (r)
Case D	Cape only (i)
Case E	Coastal canyon only (i)
Case F	Both cape and coastal canyon included (i)

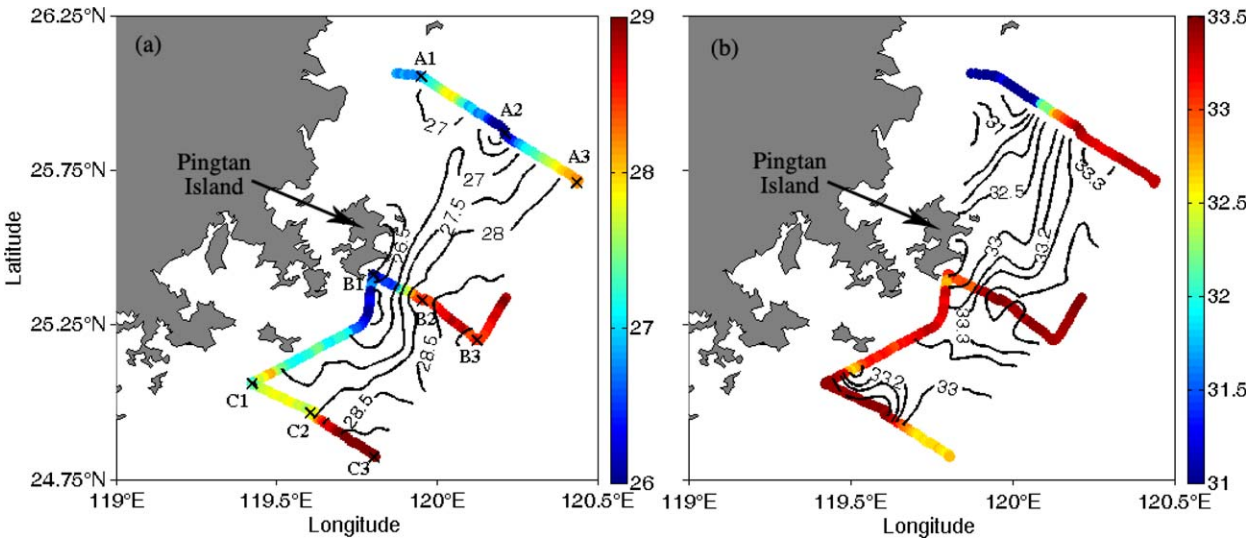

Figure 4. (a) Temperature (°C) and (b) salinity (psu) along the cruise route off Pingtan Island. The contour lines are spatial distributions of temperature and salinity interpolated from the data along the cruise route. The crosses represent sampling stations.

Penghu Channel. These three sections capture the upwelling features in the northern TWS, while the freshwater affects the nearshore region in the surface layer of Sections A and B.

3.2. Remote Sensing Results

The 8 day averaged SST data with fewer cloud coverage make them more suitable to analyze upwelling intensity using the Fuzzy c-Means clustering (FCM) method. Details in applying the FCM method on upwelling area detection are given in Appendix A. Intensive upwelling appears in July and August in the northern TWS. As an example of testing the application of FCM method in identifying upwelling areas, Figure 6 shows the 8 day averaged SST and the corresponding FCM image with cluster $c = 4$ off the northern TWS in 12–19 July 2005. The satellite SST image shows a large cold upwelling area along the coast, which is characterized by temperature drop of $>2°C$ from the ambient sea water. The FCM image shows that the upwelled water is represented by the greenish band, and the ambient sea water with higher temperature is colored as dark red, yellow, and blue. The strip-shaped upwelling region in Class 2 water in FCM image is very similar to that in the SST image in Figure 6a, indicating a successful application of the FCM algorithm in classifying upwelling area.

With perturbations by winds and currents, the upwelling may develop or decay. The distribution of cold-water area is also affected by coastline geometry and bottom topography. When the upwelling areas in Class 2 water are identified from the SST images, statistical analysis on the climatological spatial distribution of upwelling in summer is computed. Figure 7a shows the upwelling probability pattern by overlying individual upwelling area derived from 88 FCM images in July and August of 2002–2012. The map presents that upwelling develops along the coast with a probability in the range of 0.2–0.8. Two obvious upwelling cores exist in the northern TWS. One is located off Pingtan Island, and the other is located off the Sansha Bay. The upwelling probability in the cores is greater than 0.7, demonstrating that upwelling frequently occurs in these two regions. Figure 7 shows that the maximum upwelling probability in the cross-shore direction along the coast approximately runs along the 25 m isobath, probably due to the cold subsurface water preferably outcropping at this depth. The different offshore developments of upwelling band make the probability decrease seaward. The upwelling probability also decreases coastward because of mixing effect and upwelling shut-down over the inner shelf [*Estrade et al.*, 2008]. The strip-shaped upwelling structure with two cores can be confirmed by the climatological monthly mean SST image in July averaged from 2002 to 2012 (Figure 7b). Low temperature region appears in the northern TWS with intensified upwelling intensity off Pingtan Island and the Sansha Bay. The SST in the upwelling band is $\sim$1°C lower than the ambient non-upwelled water, and it is $\sim$1.5°C lower in the two upwelling cores. Climatological monthly mean wind

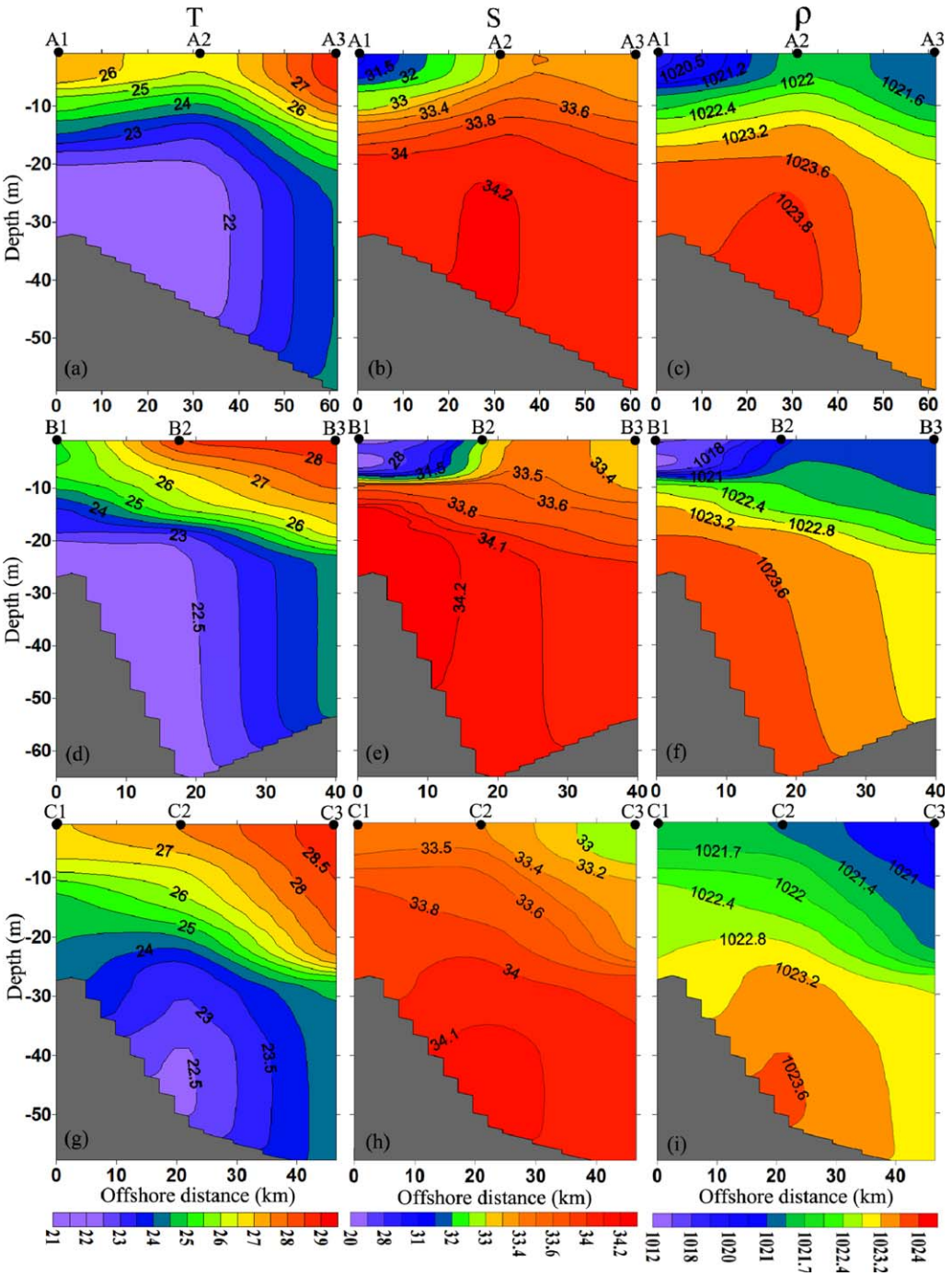

Figure 5. Temperature (°C), salinity (psu), and density (kg m^{-3}) distributions along Sections A, B, and C on 6 July 2012.

averaged in the period of 2000–2008 shows that the southerly monsoon prevails in the northern TWS in July. The southerly wind drives the surface Ekman flow offshore, and is favorable for the coastal upwelling.

3.3. Model Results

The general patterns of simulated surface flow and SST in July are shown in Figure 8a. The surface water generally flows northeastward, while the coastal current is controlled by the coastline geometry and bathymetry over the shallow shelf. The velocity increases offshore. As the climatological southerly wind continuously blows on the surface, a strip of cold upwelling band appears along the coast, and the upwelling is

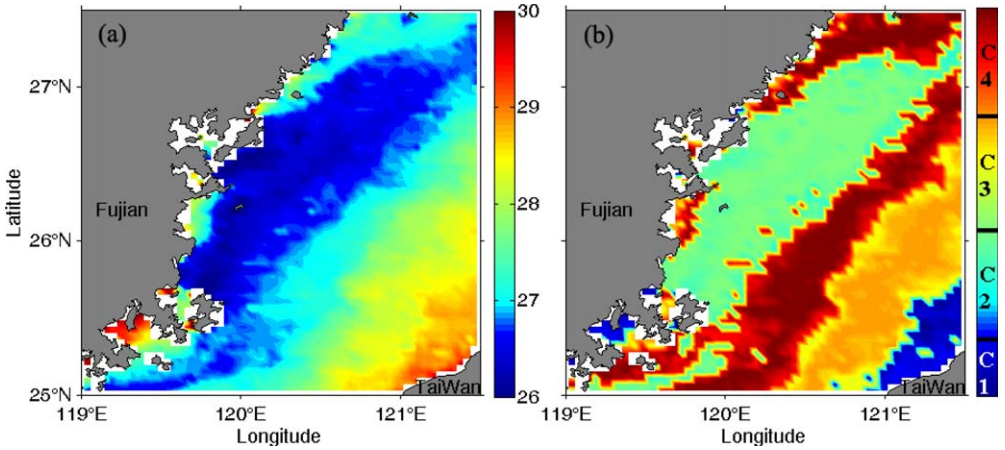

Figure 6. (a) Eight day averaged SST (°C) image off the northern Taiwan Strait on 12–19 July 2005; (b) the corresponding FCM 4-partition image. C1–C4 means Class 1–Class 4 waters.

intensified downstream of Pingtan Island with temperature cooler than 25°C. The model simulation reproduces the upwelling characteristics in the northern TWS. Since the SST from the remote sensing is the skin temperature, the SST from the numerical model result is lower than that of remote sensing data. Figure 8b shows the velocity vectors superimposed on temperature in the bottom layer. The bottom current deflects onshore due to the bottom topography and friction as it flows northeastward. The current from the Wuqiu Depression brings deep cold water northward, and curves anticlockwise around Pingtan Island. A coastal canyon, i.e., a topographic depression, off the Sansha Bay makes a channel for the bottom current to advect shoreward. After the bottom current transports onshore off the Sansha Bay, it veers northward climbing up the shelf over the shallow bottom topography.

The simulated temperature profiles on 13 July along Sections A–C and the mean temperature in July along Section P (denoted in Figure 8a) are shown in Figure 9. Similar to the observations, stratification is enhanced far offshore, while upwelling breaks the thermal barrier in the coastal region, i.e., cold water upwells to the surface at ~10 km in Section A, isotherms uplift shoreward in Sections B and C, implying shoreward advection of cold water. Cold bottom water from the Wuqiu Depression is confined beneath the surface mixed layer. The temperature profile along the cross-shore Section P off the Sansha Bay indicates a transport of bottom water upward from coastal canyon leading the 26°C isotherm to outcrop at 10 km offshore. The numerical model results are similar to the cruise observations, although discrepancies exist between the two, because the model is forced by the climatological monthly mean wind, while the in situ observations

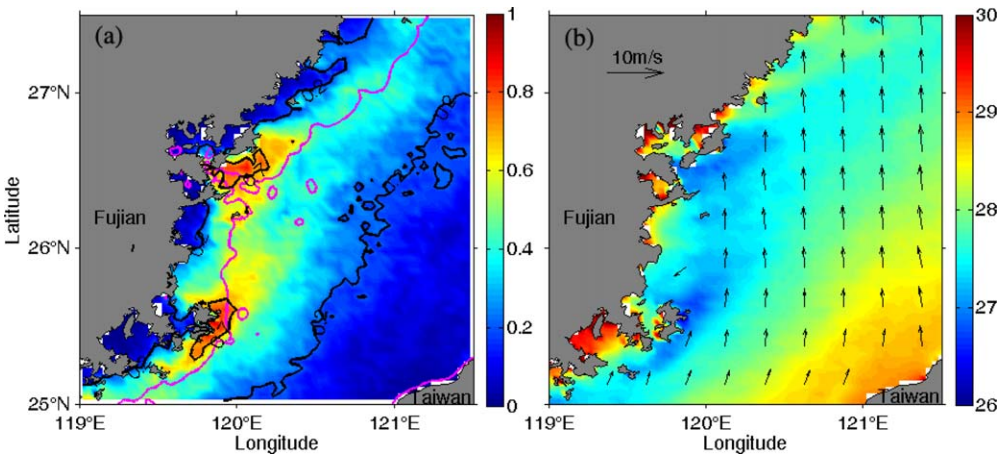

Figure 7. (a) Upwelling probability distribution in the northern Taiwan Strait. The purple contour marks the 25 m isobath. (b) Climatological monthly mean SST (°C) and wind fields in July.

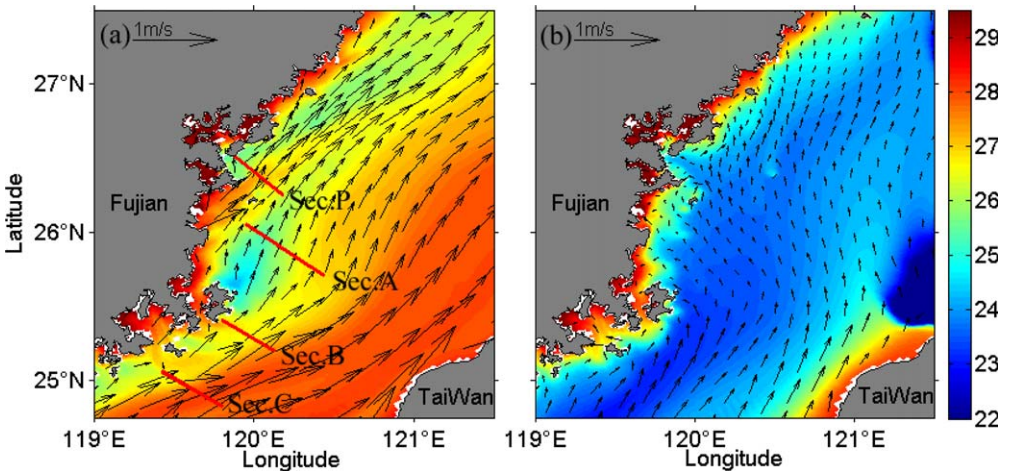

Figure 8. Model results of monthly mean temperature (°C) and velocity vectors (m s^{-1}) for the (a) surface layer and (b) bottom layer in July. The red lines mark Sections P, A, B, and C.

reflect synoptic-scale features. In the next subsections, this model is used to explore the tidal and wind effects on the upwelling features in the northern TWS.

4. Mechanisms of Upwelling

4.1. Effect of Tides

The tides in the northern TWS are characterized by semidiurnal tide with its maximum amplitude located in the area between Pingtan Island and the Meizhou Bay [*Cui et al*., 2008]. Many studies described that strong

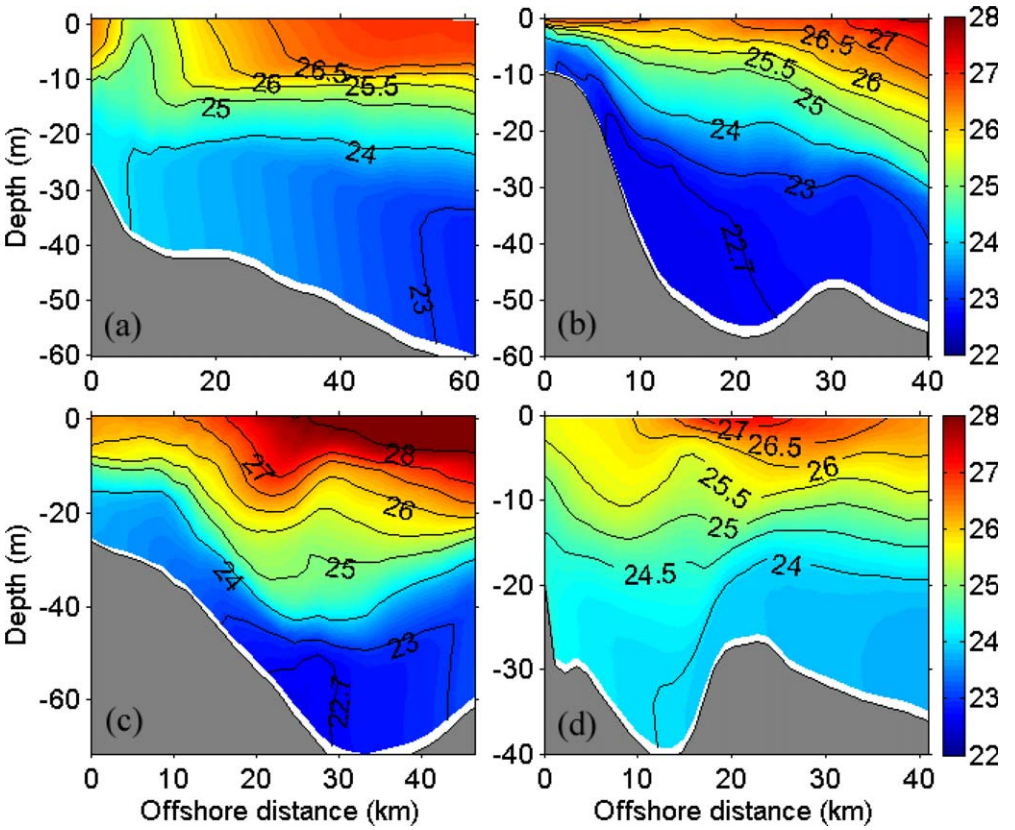

Figure 9. Vertical profiles of temperature (°C) along (a) Section A, (b) Section B, (c) Section C, and (d) Section P. Note the depths and the distances differ for these panels.

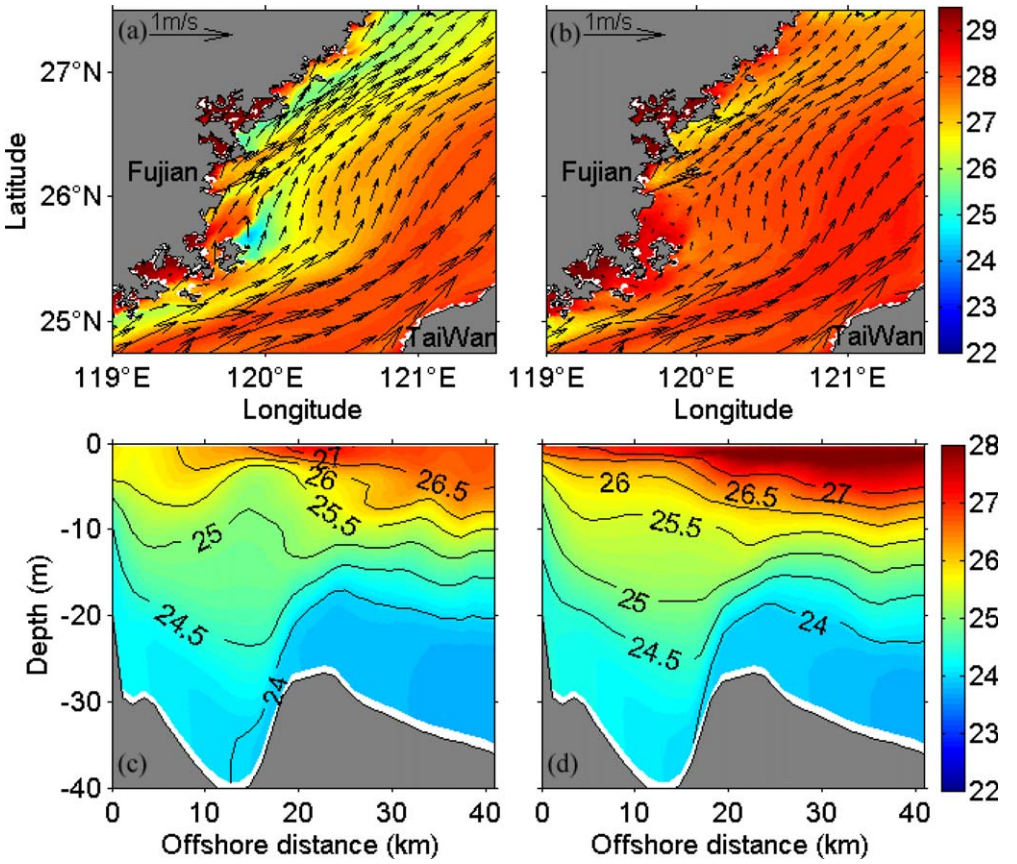

Figure 10. Surface temperature (°C) and velocity (vectors; m s^{-1}) in (a) Case B and (b) Case C. Vertical profiles of temperature for Section P in (c) Case B and (d) Case C.

tidal mixing can induce upwelling and affect vertical volume transport [e.g., *Tee et al.*, 1993; *Kurapov et al.*, 2010]. Tidal mixing diffuses the subsurface cold water in the Taiwan Bank forming upwelling there all year round [*Jiang et al.*, 2011]. To test whether the tides are important in the northern TWS, a numerical experiment of Case B without tides is carried out. Figure 10a shows the SST in July in Case B. The upwelling band with lower temperature lee of Pingtan Island and off the Sansha Bay still exists, which has a similar structure to that in Case A with tides (Figure 8a). As for the temperature profile in Section P, there is no obvious difference in temperature structures, whether the tidal effect exists or not (Figure 9d versus Figure 10c). Since tides are vigorous in the TWS, to highlight its effect, the SST difference in July between Case A and Case B and surface tidal residual current are shown in Figure 11. Positive values of SST

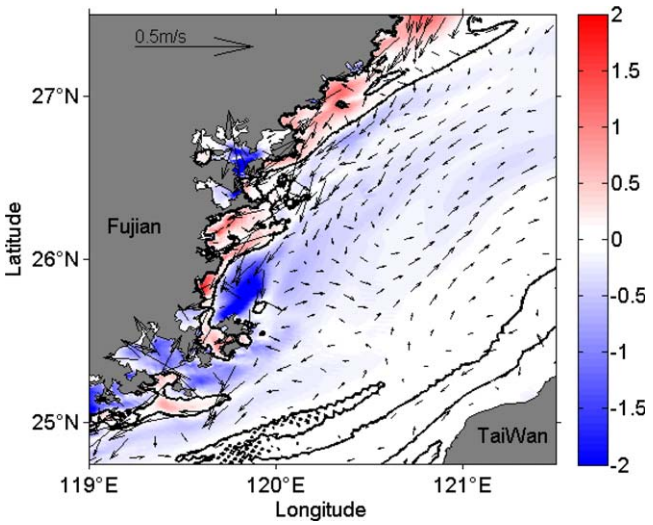

Figure 11. (a) Surface temperature difference (°C) between Case A and Case B. The thick contours mark the zero value. Arrows (vectors; m s^{-1}) indicate the surface tidal residual current.

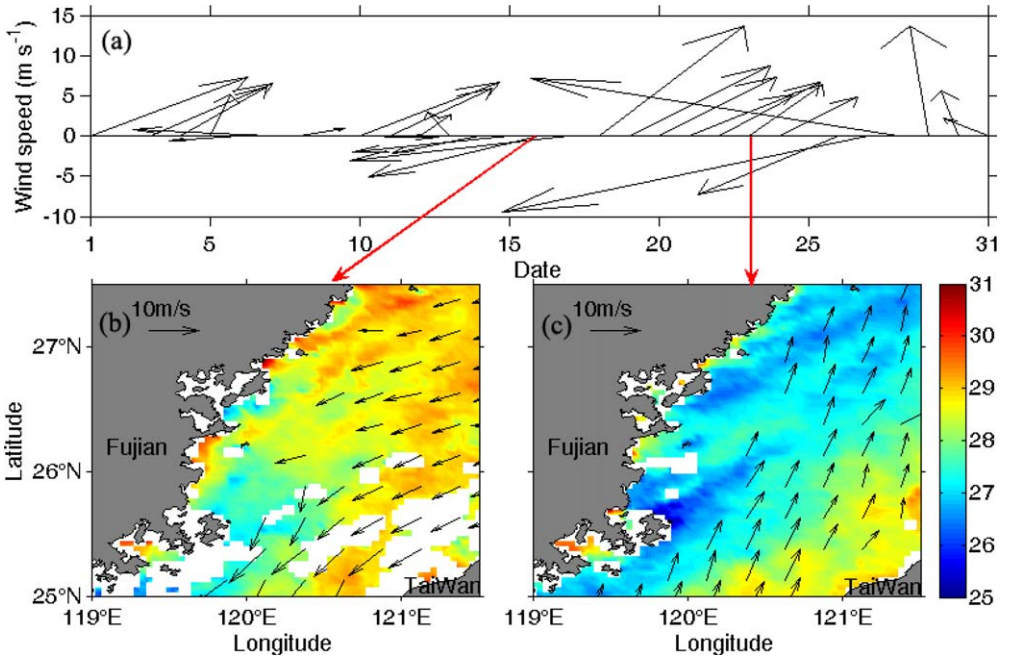

Figure 12. (a) Stick diagram of wind velocity (m s^{-1}) averaged over the study area in July 2008. (b) Upwelling unfavorable wind and SST (°C) on 16 July 2008 and (c) upwelling favorable wind and SST (°C) on 23 July 2008.

difference stretch along the coast, meaning that the SST is warmer in the shallow water in the normal case with tides. Negative values of SST difference exist farther away off the coast, especially in the shallow water region lee of Pingtan Island. The surface tidal residual current moves southwestward near the coast, turns anticlockwise northern off Pingtan Island, and veers northeastward over the outer shelf with a magnitude of ~0.1 m s^{-1}, much less than that of the circulation (~0.5 m s^{-1} in Figure 10a). Therefore, the tides are not the main reason for the upwelling in the northern TWS, but they alter the upwelling intensity locally, especially around Pingtan Island where intense tidal activity exists.

4.2. Effect of Wind

On the basis of Case B, the wind is removed in the study region in Case C, to investigate the mechanism of the cold upwelling strip off the coast. Now, the water column is only forced by the currents from the TWS. Figure 10b displays the SST and surface current accordingly. The current is weaker in the absence of wind forcing. The upwelling band off the coast and the upwelling core off Pingtan Island are no longer there, leaving a slightly cold patch off the Sansha Bay. These indicate that the cold upwelling band in the remote sensing data in summer, which often extends ~100 km off the coast, is driven by the southerly wind. The northward-flowing current still exists at the Wuqiu Depression, but the upwelling core downstream of Pingtan Island disappears, implying the importance of wind-driven current on its formation. The cold patch off the Sansha Bay is supposedly induced by the interaction of the current and the topographic depression there. Temperature profile in Section P shows that the 26°C isotherm tilts slightly up onshore by the current, but do not outcrop because of the absence of wind mixing and surface Ekman offshore transport (Figure 10d).

The sensitivity of the upwelling in the northern TWS to wind can also be verified by the remote sensing data. Although the climatological monthly mean wind is upwelling favorable in July in the northern TWS, the wind direction shifts back and forth at the synoptic scale. The QuikSCAT wind stick diagram in July 2008 shows that the wind direction and magnitude are changeable (Figure 12a). The upwelling favorable and unfavorable winds oscillate in a time scale of 4–7 days. The abnormally large wind speed in 27–28 July was related to the Typhoon, Fung-Wong. After the northeasterly wind blew for 3 days, the upwelling strip was no longer well developed, leaving two patches of cold areas off Pingtan Island and the Sansha Bay (Figure 12b). Two days later, the southwesterly wind prevailed over the northern TWS. With upwelling favorable wind lasting 6 days, a large cold water area covered the coastal region extending ~100 km offshore (Figure

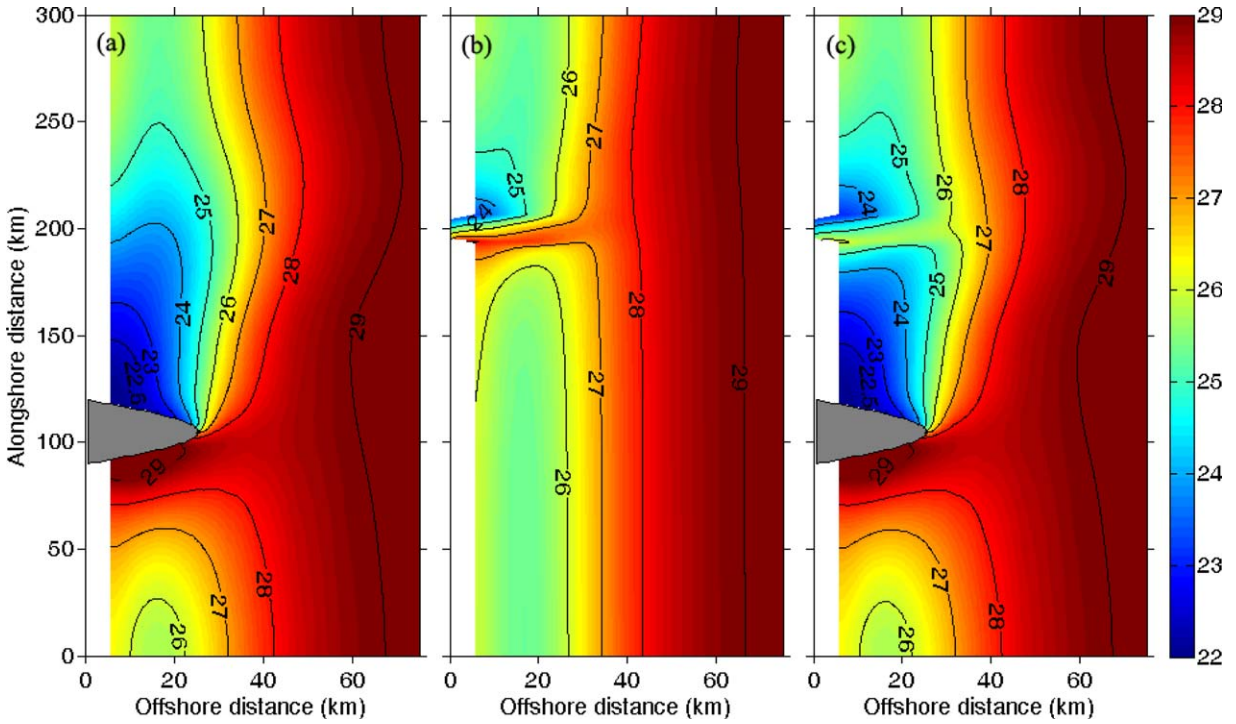

Figure 13. Distribution of temperature (°C) at 10 m depth in the cases with (a) only a cape, (b) only a canyon, and (c) both. The canyon axis is located at 200 km alongshore.

12c). Compared to the northeasterly wind, the southwesterly wind produces pronouncedly stronger upwelling, especially off Pingtan Island. Therefore, the alongshore wind is an important dynamical factor on summer upwelling in the northern TWS.

4.3. Effects of Cape and Coastal Canyon

In the idealized Case D, the model is set up with a cape on the sloping shelf, which is analogous to the geography in the northern TWS with landform of Pingtan Island protruding seaward. After the uniform wind of $\tau = 0.04$ N m^{-2} blows on the surface for 10 days, cold sea water appears along the coast at 10 m depth, especially strong downstream of the cape (Figure 13a). Influenced by the cape, the temperature drop downstream of the cape reaches 6.5°C, implying that this water mass is originated at least from 30 m depth, while the temperature upstream of the cape is not impacted by the cooling effect.

In canyon-only Case E with topography parameters comparable to that off the Sansha Bay, the temperature over and around the canyon is rearranged by the canyon topography (Figure 13b). The canyon triggers warm water on the upstream side in the south and cold water on the downstream side in the north. In Case F where the two terrains are combined, two upwelling cores are apparent downstream of the cape and canyon (Figure 13c). A cold band is cut off on the upstream side of the cape and canyon. The upwelling core of the canyon is stronger than that in Case D, meaning that the intensified upwelling downstream of the canyon is also influenced by the presence of the cape. These two cold upwelling patches correspond to the two upwelling cores off Pingtan Island and the Sansha Bay shown in Figure 7b.

The reasons for the upwelling cores downstream of the cape and coastal canyon are further studied. After 10 days of upwelling favorable wind, the sea level and coastal circulation are modified near the cape and canyon (Figure 14). The sea level drops 23–25.5 cm near the coast, which produces the northward geostrophic current ~0.3 m s^{-1}. The cape distorts the pressure contours, decreasing pressure gradient in the upstream and increasing pressure gradient off the cape head and in the downstream, corresponding to the weakened horizontal velocity in the upstream and strong upwelling jet off the cape head and in the downstream (Figure 14a). The current turns cyclonically around the cape, producing positive vorticity off the cape. In response to the variation of the ocean circulation, the vertical velocity at 10 m depth shows a large

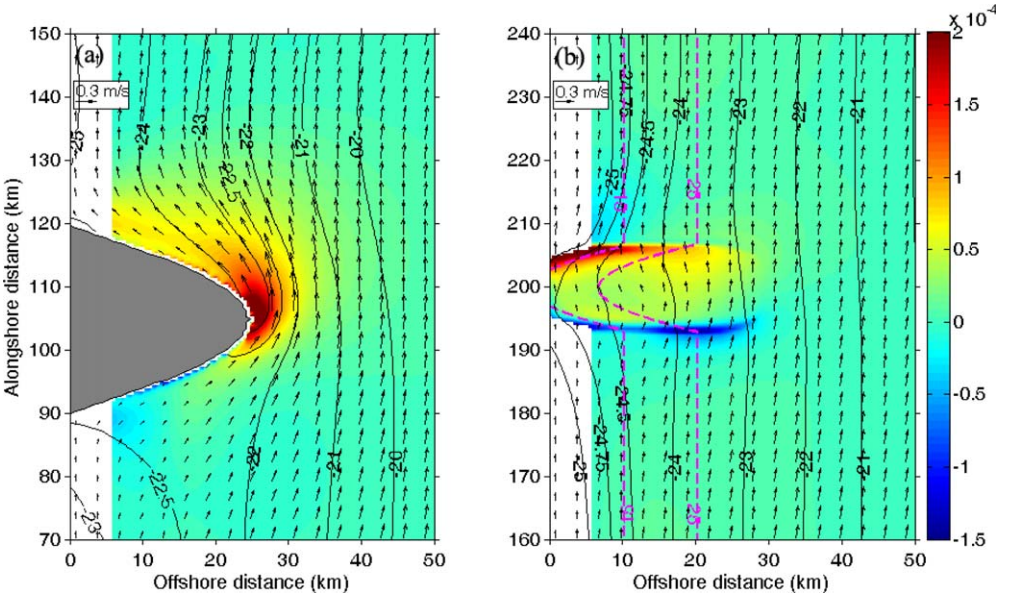

Figure 14. Surface flow (vectors) overlay on top of the vertical velocity (m s^{-1}; color shading) at 10 m depth in the cases with (a) only a cape and (b) only a canyon. Black contours show the sea level (cm; negative values off the coast), and purple dashed contours are the 15 and 25 m isobaths. The canyon axis is located at 200 km alongshore.

area of positive vertical velocity off the cape head and in the downstream area. In the upstream corner of the cape, there is a downwelling area, corresponding to the warmer water there (Figure 13a). The maximum vertical velocity appears off the cape head, but the temperature there does not change much, because the water mass is originated from the warm water upstream of the cape. The coldest water appears in the nearshore downstream of the cape, because this water is advected onshore in the manner of being continually pumped up from the head of the cape to the downstream.

Figure 14b shows the vertical velocity at 10 m depth together with the sea level and surface flow field in the case with a coastal canyon. The sea level contour is sparse over the canyon, meaning that the pressure gradient decreases so that the geostrophic current weakens. The surface currents do not follow the pressure contours and isobaths over the canyon. The currents turn cyclonically into the upstream of the canyon and anticyclonically out the downstream of the canyon. Correspondingly, the vorticity is positive in the upstream and negative in the downstream (not shown). A strong narrow downwelling area is found in the upstream rim of the canyon, while upwelling dominates over most of the canyon topography region, especially strong in the downstream rim with a strength one magnitude larger than that over the continental shelf. Cold subsurface water advects to the head of canyon, and intensively upwells downstream of the canyon, generating cold upwelled water there (Figure 13b).

To interpret the spatial distribution of vertical velocity under the influence of the cape and canyon, the vorticity equation (5) is adopted. *Arthur* [1965] showed the importance of RVC in horizontal velocity divergence off a cape, but did not show more spatial distribution. The vorticity equation is applied to Case D (with cape) and Case E (with coastal canyon). The effects of RVC and FDV on vertical velocity in these two cases are analyzed. Figure 15a displays the vertical velocity due to RVC at 10 m depth in Case D, which is computed from the first term in equation (5). Negative value is found upstream of the cape, and positive value is found downstream adjacent to the cape, followed by negative value further north. The flow field at 10 m depth is similar to that at the surface, and the magnitude of horizontal velocity at 10 m depth decreases comparing to that at the surface. The vertical velocity field by FDV (second term) at 10 m depth shows that the cape is encircled by negative value around the cape and positive value outward (Figure 15b). A combination of vertical velocities by RVC and FDV matches the vertical velocity direct output from the model result (Figure 15c), and the slight differences are due to the neglected $\partial\zeta/\partial t$ and other small terms described in section 2.2. Upwelling exists downstream of the cape, and extends upstream as a tongue to the outward of the downwelling region, although warm water presents there due to the mixing with the

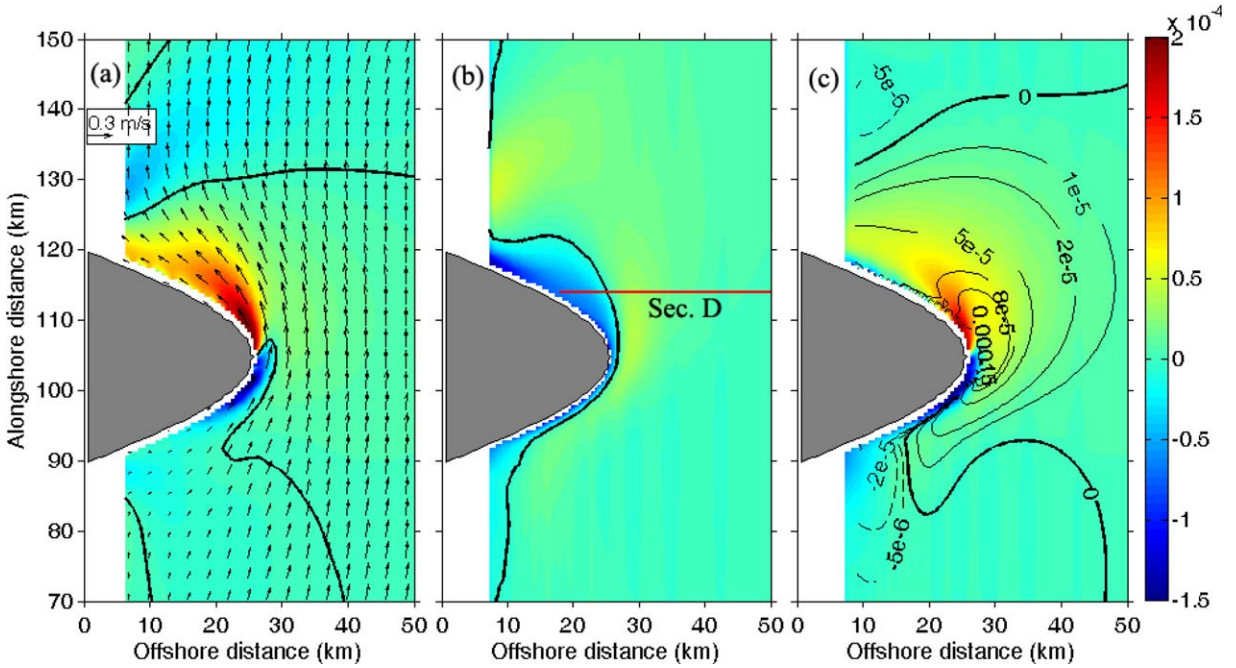

Figure 15. (a) Vertical velocity (m s^{-1}) at 10 m depth for the case with a cape induced by the RVC (first term) and horizontal velocity vectors. (b) Vertical velocity induced by FDV (second term) at 10 m depth. The red line marks Section D. (c) Combination of the two vertical velocities (color shading), where contours show the vertical velocity at 10 m depth from the model result. Note that the vertical velocity from the model result is calculated using the continuity equation. The thick black contours mark the zero vertical velocity.

warm water from the downwelling region. Comparing to the vertical velocity field induced by relative vorticity change, it is found that RVC dominates in terms of determining the vertical velocity off the cape. As a consequence, the magnitude and spatial distribution of vertical velocity off the cape can be approximately estimated by RVC.

The same method is used to analyze Case E (with coastal canyon). Vertical velocity due to RVC shows that it is positive over most of the canyon topography, except for the negative value over the upstream rim of the canyon (Figure 16a). A large negative value is also found in the northern corner out of the canyon. The flow at 10 m depth veers toward the head of canyon in the upstream, and deflects offshore in the downstream. The horizontal velocity is smaller at the head of canyon comparing to that in the canyon mouth. The vertical velocity by FDV at 10 m depth shows alternating signs in and around the canyon (Figure 16b). Over the canyon, the vertical velocity exhibits a skewed symmetry with positive value upstream and negative value downstream. A combination of vertical velocities induced by RVC and FDV matches well the vertical velocity from the model result over and around the canyon in Case E (Figure 16c). The vertical velocity is negative on the flank outside the canyon, and is positive over the canyon, except for a strong narrow downwelling band over the upstream rim of the canyon. Similarly to the case with a cape, RVC induced by the coastal canyon plays a key role in determining the vertical velocity distribution over and around the canyon.

Taking the vertical velocity calculated from the continuity equation as a benchmark, diagnostic vertical velocity by the two terms in equation (5) is analyzed (Figure 17). In the cross-shore Section D (location shown in Figure 15b) downstream of the cape, RVC overwhelms FDV in determining vertical velocity at 20−27 km offshore, and they have similar strength further offshore. The vertical velocity by RVC shows a peak value at 23 km, producing a maximum combined vertical velocity there. Then, it gradually decreases offshore. The FDV is negative in terms of contribution to the vertical velocity in the vicinity of the cape, and becomes positive further seaward. In the alongshore Section E (location shown in Figure 16b) across the coastal canyon, the situation is more complex. Over the upstream rim of the coastal canyon, the effect of FDV is negligible, and RVC produces a negative vertical velocity peak there. The effect of FDV gradually overcomes RVC a little bit northward, but the reverse happens near the axis of the coastal canyon, which persists until the downstream rim. RVC produces a positive vertical velocity peak over the downstream rim,

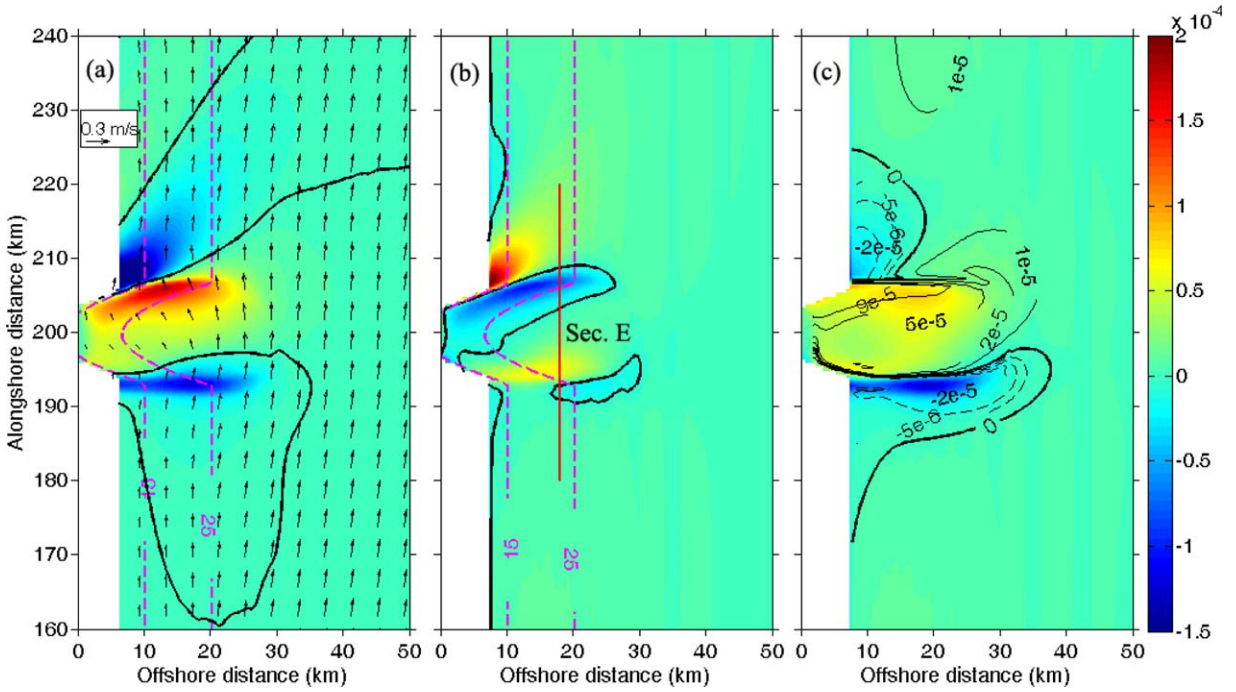

Figure 16. Same as Figure 15, except for the case with a canyon. Purple dashed contours are the 15 and 25 m isobaths. The red line in Figure 16b marks Section E. The canyon axis is located at 200 km alongshore.

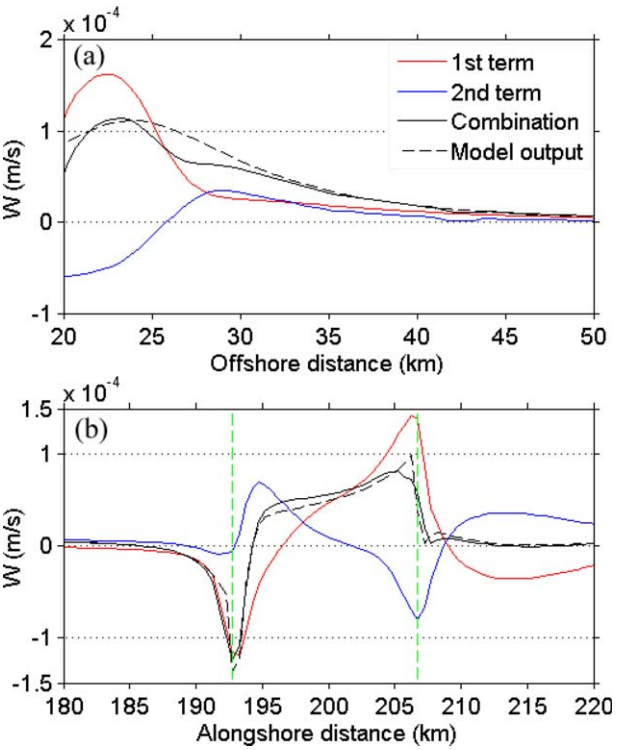

Figure 17. (a) Vertical velocity (m s^{-1}) induced by RVC, FDV, combination of the two, and direct output from the model at 10 m depth along Section D. (b) Same as (a) except along Section E. Green lines denote the locations of canyon rims.

dominating the vertical velocity there. Further north, the vertical velocity by RVC rapidly changes to negative, which is balanced by the increased vertical velocity by FDV. In both cape and coastal canyon cases, the vertical velocity calculated by combining the RVC and FDV in equation (5) matches the vertical velocity calculated from the continuity equation in terms of intensity and variation. Compared to the vertical velocity by FDV, the vertical velocity by RVC matches better with the model result; therefore, it can be used to estimate vertical velocity off the cape and over the coastal canyon.

5. Discussion

Coastal upwelling can be induced by upwelling favorable alongshore wind, Ekman pumping, tides, eddy, topography (e.g., cape, canyon), etc.

Two or more factors usually act together on the upwelling, making the coastal circulation and dynamics complicated. The synoptic scale of upwelling favorable and unfavorable winds alternately blow on the sea surface, together with the effects of cape and coastal canyon, and cause upwelling to vary spatially and temporally off the coast in the northern TWS. The research on the upwelling off Pingtan Island was active in the early 1990s, when oceanographers studied the upwelling using in situ cruise data. The available remote sensing SST data give us an opportunity to study the spatial and temporal distributions of the upwelling in the northern TWS. The authors observe a new upwelling core off the Sansha Bay in summer besides the commonly known upwelling core off Pingtan Island.

In the 1990s, oceanographers proposed different mechanisms for the upwelling in the northern TWS based on the in situ data and numerical models [e.g., *Xiao*, 1988; *Yan et al*., 1997]. In this study, remote sensing SST data reveal evidence for the important role of southerly wind on generating upwelling off the coast in the northern TWS. Numerical experiment also confirms this effect. Several oceanographers proposed that the ascending bottom topography in the northern Wuqiu Depression caused the upwelling core off Pingtan Island [*Xiao*, 1988; *Huang*, 1989a; *Huang and Weng*, 1996]. However, our results based on both observations and numerical model show that the bottom deep water from the Wuqiu Depression is confined below the thermocline, and it is hard for the deep water breaking through the thermocline as for the ascending topography in the northern part of the Wuqiu Depression, which is beneath 45 m. Only in the case of upwelling favorable wind storm lasting for several days, the bottom water from the Wuqiu Depression can break the thermal barrier, and advects onshore to the surface.

As for the role of tides, numerical experiment (Case A versus Case B) shows that it is not responsible for the cold band off the coast, but for the warming of water near shore and cooling of water outward (Figure 11). This can be explained as follows. Since the vertical eddy viscosity is increased by tides, *Chen et al*. [2013b] revealed that large eddy viscosity corresponded to a deep depth for the location of upwelling outcropping, which resulted in subsurface cold water outcropping far away from the coast in the case with tides. Under this idealized condition, upwelling occurs further offshore in the case with tides, rendering positive temperature difference near shore and negative value outward. In the real ocean, the complex topography will trigger intense tidal-topography interaction [*Jing et al*., 2012], and a strong horizontal density gradient is induced, producing a secondary circulation in the shallow water region [*Lü et al*., 2006]. The cooling effect of seawater by the tides is noticeable in the shallow region lee of Pingtan Island. This is because strong tidal currents exist off Pingtan Island, and the Simpson-Hunter parameter is small, implying strong tidal mixing there [*Zhu et al*., 2013]. Although tides contribute partly to the upwelling core in the shallow water region lee of Pingtan Island, the main mechanism for this upwelling is the circulation-cape interaction due to Pingtan Island.

Using a two-layer finite element model, *Rodrigues and Lorenzzetti* [2001] showed the importance of coastline irregularity in the formation of upwelling core off the Cabo Frio Cape. In light of the estimation of divergence off the cape along the California coast by *Arthur* [1965], equation (4) is simplified as

$$f\frac{\partial w}{\partial z}=\frac{D\zeta}{Dt}, \tag{10}$$

when the relative vorticity $\zeta \ll f$, and the FDV term is neglected. The vertical velocity below a fluid column of height H is

$$w \approx -\frac{H}{f}\frac{D\zeta}{Dt}. \tag{11}$$

Suppose a current with velocity of $V = 0.3$ m s^{-1} turns around a cape with a radius of $R = 10$ km (Figure 14a), the vorticity around the cape is $\zeta \approx V/R = 3 \times 10^{-5}$ s^{-1}. The time needed for the fluid particle flowing from the top of cape to the straight coastline downstream is $t \approx 0.5\pi R/V = 5.2 \times 10^{4}$ s. The change of relative vorticity downstream of the cape is $D\zeta/Dt = -5.8 \times 10^{-10}$ s^{-2}. In the case of water column with a depth of $H = 25$ m around the cape, the vertical velocity downstream of the cape is $w_{25} \approx 2.4 \times 10^{-4}$ m s^{-1}. The magnitude of this value is coincident with the magnitude of vertical velocity obtained from the

model result (Case D; Figure 14a). Meanwhile, the vertical velocity induced by offshore Ekman transport is estimated in the way by *Estrade et al*. [2008], that is, $w = \tau/(\rho f L) = \tau\alpha/(0.75\pi\rho\sqrt{2A_z f}) = 1.9 \times 10^{-5}$ m s^{-1}, where L is the cross-shore width of surface Ekman divergence, approximately one magnitude smaller than the vertical velocity downstream of cape. Therefore, the traditional calculation of vertical velocity from Ekman transport theory underestimates the vertical velocity downstream of cape. Even in the upwelling unfavorable wind condition, the positive vertical velocity by preponderant cape effect downstream of Pingtan Island induces a cold patch in satellite SST image (Figure 12b).

Coastal canyon shares some similar dynamics and differences to a submarine canyon. The water is driven into the submarine canyon because of the unbalanced pressure gradient by the tilted free surface and reduction of alongshore flow over the submarine canyon [*She and Klinck*, 2000]. The onshore pressure gradient is supposed to accelerate the flow into the coastal canyon in the upstream (it does in submarine canyon case) [see *Klinck*, 1996, Figure 4], but in the coastal canyon case flow decelerates to the head of canyon mainly because of the effect of shallow water depth (Figure 16a). Unlike the submarine canyon case that the water near the head of canyon is flooded upward onto the shelf, all of the water toward the head of coastal canyon is deflected offshore in the downstream. *Freeland and Denman* [1982] suggested that the up-canyon flow is due to the cross-shelf geostrophic pressure gradient, while *Kämpf* [2006] claimed that it is caused by the rapid geostrophic adjustment to the barotropic pressure gradients across the submarine canyon. As the water enters the canyon in the upstream, the vortex tube stretches generating cyclonic vorticity. The stretching is strong enough to form a cyclonic eddy over the submarine canyon rim [*She and Klinck*, 2000; *Allen and Hickey*, 2010], while only a meander is generated over coastal canyon. This is because stratification is strong in surface layer, and it is commonly accepted that strong stratification inside the canyon is a barrier to the canyon topographic effect [*Klinck*, 1996; *Kämpf*, 2007]. This results in smaller vorticity change and upwelling flux in coastal canyon case than that in submarine canyon case. In general, comparing to the submarine canyon case, weakening circulation, strong stratification and shallow topography depression over coastal canyon is unfavorable for the canyon upwelling flux. However, the effect of coastal canyon on forming an upwelling core is comparable to that induced by a cape (Figure 7b). In the coastal canyon region, surface Ekman transport directly acts upon the up-canyon flow, bringing nutrient to the euphotic zone. The coastal canyon effects on surface mass exchange, mixing and coastal ecosystems may be more important than that over a submarine canyon. Although upwelling is stronger over a submarine canyon than elsewhere on the shelf, surface current often forms a barrier to limit the upwelling, so only with the aid of strong upwelling favorable wind can nutrients be brought over a submarine canyon to the euphotic zone [*Rennie et al*., 2009]. Even right-bounded flow (flow with coast on the right; downwelling case) leads to upwelling downstream of the canyon, although its strength is weaker comparing to the upwelling case [*Klinck*, 1996]. This is the reason for the cold patch off the Sansha Bay observed from the remote sensing SST data under upwelling unfavorable wind condition (Figure 12b).

For barotropic quasigeostrophic incompressible flow, fluid column follows the fundamental rule of potential vorticity conservation

$$\frac{d}{dt}\left(\frac{f+\zeta}{H}\right)=0. \tag{12}$$

Encountering with a cape, the current turns offshore upstream, and the vortex tube stretches, resulting in $d\zeta/dt > 0$ under the conservation of potential vorticity. According to equation (11), the vertical velocity induced by RVC is negative (Figure 15a). Similarly, as the upwelling jet deflects onshore downstream of the cape, the compressing vortex tube produces positive vertical velocity by RVC. Further north, upwelling jet veers offshore, which is the same to the condition upstream of the cape. In the upstream of a coastal canyon, when the current flows northward, the vortex tube stretches with the deepening depth, resulting in $d\zeta/dt > 0$ under the conservation of potential vorticity (Figure 16a). The vertical velocity related to RVC is then negative. The situation reverses downstream of the canyon. After the bottom water upwells downstream of the canyon, it deflects offshore in the corner outside of the canyon. The vortex tube stretches, producing negative vertical velocity. The variations of pressure gradient and water depth along streamlines off the cape or over the coastal canyon regions modify the relative vorticity, and mainly produce intensified upwelling and downwelling there.

Using an idealized numerical model, *Kämpf* [2012] pointed out that a stationary topographic Rossby wave was created with a wavelength of ~67 km downstream of the cape. Comparing to Case E, the upwelling downstream of the canyon in Case F is stronger, probably due to this wave triggered by the cape. The length scale of the wave is comparable to the distance between the coastal canyon off the Sansha Bay and Pingtan Island. To understand whether the topographic Rossby wave, which occurs in the idealized numerical model, has an influence on the upwelling core off the Sansha Bay, we need more in situ observations and numerical experiments with realistic topography and dynamical conditions.

6. Summary

Hydrographic cruise data and remote sensing data, combined with numerical model, are used to investigate the climatological upwelling features in the northern TWS in summer. In situ data show that upwelling exists in a region off Pingtan Island in July 2012. Nearshore bottom cold water from the Wuqiu Depression is confined below thermocline. Climatological monthly mean SST data in 2002–2012 from remote sensing provide further evidence for the upwelling with lower temperature off the coast. A strip of upwelling with two cores, which are located off Pingtan Island and the Sansha Bay, appears in the northern TWS. After the cold upwelling areas from remote sensing SST images are differentiated using the FCM method, spatial distribution of the upwelling probability pattern in the northern TWS in summer is obtained. The probability map shows that upwelling appears at least half the time in July and August, and the two cores' probability is greater than 0.7. The QuikSCAT climatological monthly mean wind shows that southerly wind prevails in July in the study area. Forced by the climatological wind, the numerical model produces similar temperature distributions on the surface and in cross-shore sections as those of the remote sensing and in situ data.

Remote sensing data and numerical model with realistic and idealized conditions are used to explore the mechanisms for the observed upwelling features. Model results show that tidal mixing is not negligible for the upwelling in the shallow water region, which accounts partly for the existence of the upwelling core lee of Pingtan Island. Surface tidal residual current moves southward off the coast and makes a *U*-turn to the north off Pingtan Island. Comparing to the SST in upwelling favorable wind condition, the disappearance of the cold band off the coast in the case of no wind in the study area (Case C) and the unfavorable wind condition in remote sensing data suggest that the southerly wind is responsible for the strip of upwelling in the northern TWS.

To further explore the main reasons for two upwelling cores off Pingtan Island and the Sansha Bay, an idealized numerical experiment is set up with a coastal canyon downstream of a cape over a sloping shelf, whose geographic parameters are comparable to those in the northern TWS. Model result displays two upwelling cores in the upwelling band off the coast, which are located downstream of the cape and coastal canyon, separately. Cyclonic current around the cape produces negative vertical velocity related to RVC upstream of the cape and the reverse situation downstream. Vertical velocity by FDV is negative adjacent to the cape and positive outward. As the flow cyclonically veers into the coastal canyon, the RVC produces strong negative vertical velocity over the upstream rim of canyon, and changes to positive value over the canyon axis and in the downstream area, followed by negative value in the northern corner outside the canyon when the flow deflects offshore. The vertical velocity by FDV is positive upstream of the canyon and negative downstream. Idealized model results indicate that RVC is the dominant effect contributing to the vertical velocity off the cape, and over and around the coastal canyon. This gives us another method to estimate the spatial distribution of vertical velocity in cape and canyon topography regions. Enhanced vertical velocities downstream of the cape and canyon are responsible for the two upwelling cores with lower temperature in Case F, and are the main mechanisms for the observations in the northern TWS. Therefore, the southerly wind drives the upwelling band off the coast in the northern TWS, while the upwelling intensity is largely influenced by the local coastline geometry and topography, mainly by RVC induced by Pingtan Island and the coastal canyon topography off the Sansha Bay to keep the potential vorticity conservation.

Appendix A: Upwelling Area Identification

To identify the spatial distribution of upwelling features, it is essential to differentiate the upwelling region from ambient seawater. The upwelling region is often characterized by lower sea surface temperature. Many researchers use a threshold, for instance 2°C lower than averaged temperature from ambient water,

to identify the upwelling region, which obviously is subjective. To avoid this subjectivity, automatic identification method is used to identify the upwelling areas. The FCM method provides a degree that each pixel belongs to the clusters considering the ambiguity of the boundaries, and is used in image segmentation widely [*Bezdek and Pal*, 1992; *Bezdek et al*., 1999]. *Sousa et al.* [2008] and *Chen et al.* [2012] had successfully applied the FCM method in identifying the upwelling regions on SST images. Similarly, the FCM method is applied to differentiate the upwelling region from the MODIS SST images in the northern TWS. The FCM algorithm aims at the minimization of an objective function J_m by performing iteration. It is defined by *Dunn* [1973] as

$$J_m(U,V;X)=\sum_{i=1}^{c}\sum_{k=1}^{n}(u_{ik})^m d^2(x_k,v_i), \tag{A1}$$

where $u_{ik}=\dfrac{1}{\sum_{j=1}^{c}\left[\dfrac{d^2(x_k,v_i)}{d^2(x_k,v_j)}\right]^{\frac{1}{m-1}}}\in[0,1]$ ($i=1,2,\ldots,c$; $k=1,2,\ldots,n$) are fuzzy membership values, $m=2$ is the weight exponent, and d^2 is the squared Euclidean distance by the form

$$d^2(x_k,v_i)=||x_k-v_i||_A^2=||(x_k-v_i)||^T A(x_k-v_i), \tag{A2}$$

where x_k represents data points and $v_i=\dfrac{\sum_{k=1}^{n}(u_{ik})^m x_k}{\sum_{k=1}^{n}(u_{ik})^m}$ ($i=1,2,\ldots,c$) is the cluster prototypes. In this study, x_k is SST in each pixel and v_i is the average weighted temperature pertaining to cluster *i*. After iterating until $\|v_i^{t+1}-v_i^t\|\le\varepsilon$, a small positive value, the FCM algorithm strictly converges to the minimization of the objective function J_m.

Acknowledgments

This work was supported by grant (2013CB955704) from the National Major Scientific Research Program of China, grant (41076001) from the Natural Science Foundation of China (NSFC), and grant (U1305231) from NSFC and Fujian Province. This work was supervised by Yuwu Jiang during his visit at University of Delaware while on sabbatical. We are grateful for the improvement of presentation by Z. J. Yu. We also thank the two anonymous reviewers for helpful comments on the manuscript.

References

Allen, S. E. (1996), Topographically generated, subinertial flows within a finite length canyon, *J. Phys. Oceanogr.*, *26*, 1608–1632.

Allen, S. E., and B. M. Hickey (2010), Dynamics of advection-driven upwelling over a shelf break submarine canyon, *J. Geophys. Res.*, *115*, C08018, doi:10.1029/2009JC005731.

Arthur, R. S. (1965), On the calculation of vertical motion in eastern boundary currents from determinations of horizontal motion, *J. Geophys. Res.*, *70*, 2799–2803.

Austin, J. A., and S. J. Lentz (2002), The inner shelf response to wind-driven upwelling and downwelling, *J. Phys. Oceanogr.*, *32*, 2171–2193.

Bezdek, J. C., and S. K. Pal (1992), *Fuzzy Models for Pattern Recognition*, IEEE Press, N. Y.

Bezdek, J. C., J. Keller, R. Krishnapuram, and N. R. Pal (1999), *Fuzzy Models and Algorithms for Pattern Recognition and Image Processing*, Kluwer Acad., Boston, Mass.

Breaker, L. C., and C. N. K. Mooers (1986), Oceanic variability off the central California coast, *Prog. Oceanogr.*, *17*, 61–135.

Chen, H., J. Y. Hu, W. R. Pan, G. N. Zeng, Z. Z. Chen, Z. G. He, C. Y. Zhang, and H. Li (2001), Underway measurement of sea surface temperature and salinity in the Taiwan Straits in August, 1999 [in Chinese with English abstract], *Mar. Sci. Bull.*, *4*, 11–18.

Chen, Z. Y., X.-H. Yan, Y.-H. Jo, L. D. Jiang, and Y. W. Jiang (2012), A study of Benguela upwelling system using different upwelling indices derived from remotely sensed data, *Cont. Shelf Res.*, *45*, 27–33.

Chen, Z. Y., X.-H. Yan, Y. W. Jiang, and L. D. Jiang (2013a), Roles of shelf slope and wind on upwelling: A case study off east and west coasts of the US, *Ocean Modell.*, *69*, 136–145.

Chen, Z. Y., X.-H. Yan, Y. W. Jiang, L. D. Jiang, and Y.-H. Jo (2013b), A study of cross-shore maximum upwelling intensity along the Northwest Africa coast, *J. Oceanogr.*, *69*, 443–450.

Cui, P., F. X. Zhang, and Y. W. Jiang (2008), Numerical simulation of the M2 tidal wave distribution in the Taiwan Strait [in Chinese with English abstract], *J. Xiamen Univ.*, *47*, 426–430.

Da Silva, A. M., C. C. Young, and S. Levitus (1994), *Atlas of Surface Marine Data 1994*, vol. 1, *Algorithms and Procedures*, *NOAA Atlas NESDIS 6*, 74 pp., U.S. Dep. of Commer., NOAA, NESDIS, Washington, D. C.

Doglioli, A. M., A. Griffa, and M. G. Magaldi (2004), Numerical study of a coastal current on a steep slope in presence of a cape: The case of the Promontorio di Portofino, *J. Geophys. Res.*, *109*, C12033, doi:10.1029/2004JC002422.

Dunn, J. C. (1973), A fuzzy relative of the ISODATA process and its use in detecting compact well-separated clusters, *J. Cybern.*, *3*, 32–57.

Egbert, G. D., and S. Y. (2002), Erofeeva Efficient inverse modeling of barotropic ocean tides, *J. Atmos. Oceanic Technol.*, *19*, 183–204.

Estrade, P., P. Marchesiello, A. C. D. Verdière, and C. Roy (2008), Cross-shelf structure of coastal upwelling: A two-dimensional extension of Ekman's theory and a mechanism for inner shelf upwelling shut down, *J. Mar. Res.*, *66*, 589–616.

Flather, R. A. (1976), A tidal model of the northwest European continental shelf, *Mem. Soc. R. Sci. Liege Ser.*, *10*(6), 141–164.

Freeland, H. J., and K. L. Denman (1982), A topographically controlled upwelling center off southern Vancouver Island, *J. Mar. Res.*, *40*, 1069–1093.

Gan, J., A. Cheung, X. Guo, and L. Li (2009), Intensified upwelling over a widened shelf in the northeastern South China Sea, *J. Geophys. Res.*, *114*, C09019, doi:10.1029/2007JC004660.
Gan, J., H. Ho, and L. Liang (2013), Dynamics of intensified downwelling circulation over a widened shelf in the northeastern South China Sea, *J. Phys. Oceanogr.*, *43*, 80–94.
Hellerman, S., and M. Rosenstein (1983), Normal monthly wind stress over the world ocean with error estimates, *J. Phys. Oceanogr.*, *13*, 1093–1104.
Hu, J. Y., H. S. Hong, Z. G. He, X. B. Zhang, Z. Z. Chen, C. Y. Zhang, and H. Li (2000), Analysis on temperature and salinity of surface water in Taiwan Strait in August, 1998 [in Chinese with English abstract], *Trop. Oceanogr.*, *19*, 15–22.
Hu, J. Y., H. Kawamura, H. S. Hong, M. Suetsugu, and M. S. Lin (2001), Hydrographic and satellite observations of summertime upwelling in the Taiwan Strait: A preliminary description [in Chinese with English abstract], *Terr. Atmos. Oceanic Sci.*, *12*, 415–430.
Hu, J. Y., H. Kawamura, C. Y. Li, H. S. Hong, and Y. W. Jiang (2010), Review on current and seawater volume transport through the Taiwan Strait, *J. Oceanogr.*, *66*, 591–610.
Huang, R. X. (1989a), Upwelling in middle and north Taiwan Strait [in Chinese with English abstract], *Trans. Oceanic Limnol.*, *4*, 8–12.
Huang, R. X. (1989b), Characteristics of water temperature and salinity in north central Taiwan Strait [in Chinese with English abstract], *Mar. Sci. Mon.*, *6*, 33–38.
Huang, R. X., and X. C. Weng (1996), The characteristics and cause analyses of the upwelling in the coastal area of central Fujian [in Chinese with English abstract], *Trop. Oceanogr.*, *15*, 52–59.
Jan, S., J. Wang, C. S. Chern, and S. Y. Chao (2002), Seasonal variation of the circulation in the Taiwan Strait, *J. Mar. Syst.*, *35*, 249–268.
Jiang, L., X.-H. Yan, and L. C. Breaker (2012), Upwelling age—An indicator of local tendency for coastal upwelling, *J. Oceanogr.*, *68*, 337–344, doi:10.1007/s10872-011-0096-2.
Jiang, Y. W., F. Chai, Z. W. Wan, X. Zhang, and H. S. Hong (2011), Characteristics and mechanisms of the upwelling in the southern Taiwan Strait: A three-dimensional numerical model study, *J. Oceanogr.*, *67*, 699–708.
Jing, Z., Y. Qi, and Y. Du (2012), Persistent upwelling and front over the Sulu Ridge and their variations, *J. Geophys. Res.*, *117*, C11011, doi: 10.1029/2012JC008355.
Kämpf, J. (2006), Transient wind-driven upwelling in a submarine canyon: A process-oriented modeling study, *J. Geophys. Res.*, *111*, C11011, doi:10.1029/2006JC003497.
Kämpf, J. (2007), On the magnitude of upwelling fluxes in shelf-break canyons, *Cont. Shelf Res.*, *27*, 2211–2223.
Kämpf, J. (2012), Lee effects of localized upwelling in a shelf-break canyon, *Cont. Shelf Res.*, *42*, 78–88.
Klinck, J. M. (1996), Circulation near submarine canyons: A modeling study, *J. Geophys. Res.*, *101*, 1211–1223.
Kurapov, A. L., J. S. Allen, and G. D. Egbert (2010), Combined effects of wind-driven upwelling and internal tide on the continental shelf, *J. Phys. Oceanogr.*, *40*, 737–756.
Large, W. G., J. C. McWilliams, and S. C. Doney (1994), Oceanic vertical mixing: A review and a model with a nonlocal boundary layer parameterization, *Rev. Geophys.*, *32*, 363–403, doi:10.1029/94RG01872.
Liang, H. X. (1997), Analysis of oceanographic condition in the Taiwan Strait during summer 1994, in *Oceanography in China* 7 [in Chinese with English abstract], pp. 49–61, China Ocean Press, Beijing.
Liao, E. H., Y. W. Jiang, L. Li, H. S. Hong, and X.-H. Yan (2013), The cause of the 2008 cold disaster in the Taiwan Strait, *Ocean Modell.*, *62*, 1–10.
Lü, X., F. Qiao, C. Xia, J. Zhu, and Y. Yuan (2006), Upwelling off Yangtze River estuary in summer, *J. Geophys. Res.*, *111*, C11S08, doi:10.1029/2005JC003250.
Mason, E., F. Colas, and J. L. Pelegri (2012), A Lagrangian study tracing water parcel origins in the Canary Upwelling System, *Sci. Mar.*, *76*, 79–94.
Pringle, J. M. (2002), Enhancement of wind-driven upwelling and downwelling by alongshore bathymetric variability, *J. Phys. Oceanogr.*, *32*, 3101–3112.
Rennie, S. J., C. B. Pattiaratchi, and R. D. McCauley (2009), Numerical simulation of the circulation within the Perth Submarine Canyon, Western Australia, *Cont. Shelf Res.*, *29*, 2020–2036.
Rodrigues, R. R., and J. A. Lorenzzetti (2001), A numerical study of the effects of bottom topography and coastline geometry on the Southeast Brazilian coastal upwelling, *Cont. Shelf Res.*, *21*, 371–394.
Samelson, R., P. Barbour, J. Barth, S. Bielli, T. Boyd, D. Chelton, P. Kosro, M. Levine, and E. Skyllingstad (2002), Wind stress forcing of the Oregon coastal ocean during the 1999 upwelling season, *J. Geophys. Res.*, *107*(C5), 3034, doi:10.1029/2001JC000900.
She, J., and J. M. Klinck (2000), Flow near submarine canyons driven by constant winds, *J. Geophys. Res.*, *105*, 28,671–28,694.
Sousa, F. M., S. Nascimento, H. Casimiro, and D. Boutov (2008), Identification of upwelling areas on sea surface temperature images using fuzzy clustering, *Remote Sens. Environ.*, *112*, 2817–2823.
Tang, D. L., D. R. Kester, I.-H. Ni, H. Kawamura, and H. S. Hong (2002), Upwelling in the Taiwan Strait during the summer monsoon detected by satellite and shipboard measurements, *Remote Sens. Environ.*, *83*, 457–471.
Tee, K. T., P. C. Smith, and D. Lefaivre (1993), Topographic upwelling off Southwest Nova Scotia, *J. Phys. Oceanogr.*, *23*, 1703–1726.
Wang, D., Y. Shu, H. Xue, J. Hu, J. Chen, W. Zhuang, T. T. Zu, and J. Xu (2014), Relative contributions of local wind and topography to the coastal upwelling intensity in the northern South China Sea, *J. Geophys. Res.*, *119*, 2550–2567, doi:10.1002/2013JC009172.
Weng, X. C., Q. L. Zhang, T. Z. Yan, and C. M. Wang (1992), Analysis of water masses in the middle and northern Taiwan Strait in spring and summer [in Chinese with English abstract], *Ocean. Limnol. Sin.*, *23*, 235–244.
Williams, W. J., and E. C. Carmack (2008), Combined effect of wind-forcing and isobath divergence on upwelling at Cape Bathurst, Beaufort Sea, *J. Mar. Res.*, *66*, 645–663.
Wu, Y. C., X. C. Weng, and Y. L. Yang (1997), Analysis on causes of generation, evolution and decay process of upwelling off the western coast of Taiwan Strait [in Chinese with English abstract], *Stud. Mar. Sin.*, *38*, 53–59.
Xiao, H. (1988), Studies of coastal upwelling in western Taiwan Strait [in Chinese with English abstract], *J. Oceangr. Taiwan Strait*, *7*, 135–142.
Yan, T. Z., H. Y. Li, and G. Y. Yu (1997), Numerical study on upwelling along the Fujian coast: Three dimensional numerical simulation of upwelling in Taiwan Strait [in Chinese], *Acta Ocean. Sin.*, *19*, 12–19.
Zhu, J., J. Y. Hu, and Z. Y. Liu (2013), On summer stratification and tidal mixing in the Taiwan Strait, *Frontiers Earth Sci.*, *7*(2), 141–150.